



LAWRENCE
LIVERMORE
NATIONAL
LABORATORY

DENSITY-FUNCTIONAL STUDY OF THE U-ZR SYSTEM

A. Landa, P. Soderlind, P. Turchi

July 2, 2008

Journal of Alloys and Compounds

Disclaimer

This document was prepared as an account of work sponsored by an agency of the United States government. Neither the United States government nor Lawrence Livermore National Security, LLC, nor any of their employees makes any warranty, expressed or implied, or assumes any legal liability or responsibility for the accuracy, completeness, or usefulness of any information, apparatus, product, or process disclosed, or represents that its use would not infringe privately owned rights. Reference herein to any specific commercial product, process, or service by trade name, trademark, manufacturer, or otherwise does not necessarily constitute or imply its endorsement, recommendation, or favoring by the United States government or Lawrence Livermore National Security, LLC. The views and opinions of authors expressed herein do not necessarily state or reflect those of the United States government or Lawrence Livermore National Security, LLC, and shall not be used for advertising or product endorsement purposes.

Density-functional study of the U-Zr system

Alex Landa^{*}, Per Söderlind, and Patrice E.A. Turchi

Lawrence Livermore National Laboratory, PO Box 808, Livermore, CA 94551, USA

Abstract

Density-functional formalism is applied to study the phase equilibria in the U-Zr system. The obtained ground-state properties of the γ (bcc) and δ (C32) phases are in good agreement with experimental data. The decomposition curve for the γ -based U-Zr solutions is calculated. Our calculations confirm that experimentally observed “partial” ordering of the alloy components in the δ -UZr₂ (AlB₂) phase, in which Zr atoms occupy the “Al” position and the two “B” sites are randomly shared by the U and Zr atoms, is the most energetically favorable within the C32 structure. We argue that stabilization of the δ -UZr₂ phase relative to the α -Zr (hcp) structure is due to an increase of the Zr *d*-band occupancy that occurs when U is alloyed with Zr. A comparison with stabilization of the ω -phase (also C32) in Zr under compression is made.

Keywords: nuclear reactor materials (A); phase transitions (C); computer simulations (D).

^{*} Corresponding author. Tel.: +1 925 424 3523; fax: +1 925 422 2851. E-Mail address: landa1@llnl.gov (A. Landa)

1. Introduction

Zr-based actinide alloys, particularly U-Pu-Zr, proved to be very promising fuels for liquid metal fast breeder reactors because of their advantage in view of superior performance, reactor safety, and fuel cycle economics [1]. The main goal of fast breeder reactors is to achieve a so-called “high burn-up” fissioning all types of transuranic elements, rather than only the “fissile” isotopes splitting in the thermal reactors, thus providing an appropriate solution to spent fuel recycling and complete transmutation of long-lived minor actinides (Np, Am, and Cm), which results in creation of a closed nuclear fuel cycle with future disposition of the nuclear waste products in a single geological repository [2]. Early on, metallic fuels (pure U and Pu) have been considered because of their high thermal conductivity (with the very significant safety benefits) in comparison with oxides fuels (e.g., UPuO_2) used in thermal reactors. However, the low melting temperature of pure U, Pu, and the U-Pu alloys makes them unsuitable for high temperature applications due to the danger of penetration of molten actinides to the cladding. That is why addition of some high-melting temperature elements, such as Cr, Mo, Ti, and Zr, is considered in order to boost the liquidus curve in the U-Pu system thus enhancing thermal and mechanical stability. However, zirconium metal also possesses a unique capability to suppress interdiffusion between the nuclear fuel and stainless-steel cladding and this makes Zr a good candidate as a solver to nuclear fuels for fast breeder reactors.

In spite of the renewed interest in the Zr-based actinide alloys from the practical view point, very little has been done to understand fundamental aspects of phase

equilibria in these systems. It was established [3] that the U-Zr system is characterized by the complete solubility of the body centered cubic high-temperature phases, γ -U and β -Zr, that is usually referred to in phase diagrams by ‘ γ -phase’ solid solutions. Below $T \approx 995$ K, these solutions separate into a relatively flat miscibility gap, which ranges from about 10 to 40 at. % of Zr, and spans about 30 K below the critical point. The intermediate δ -phase is formed on cooling from the γ -phase around UZr_2 stoichiometry with the homogeneity range from 63 to 82 at. % Zr [4].

Both γ and δ phases in the U-Zr system play an important role in metallurgical reactions that occur during the nuclear burn-up. A typical U-Zr fuel rod contains about 10 wt. % of Zr (~ 23 at. %) in the γ -phase [5]. During the burn-up process, composition of U in the fuel rod decreases resulting in a subsequent increase of Zr composition. For example according to Ref. [6], the 5 at. % burn-up will cause the maximum Zr concentration to increase from ~ 23 at. % to ~ 45 at. %. It will cause redistribution of Zr within the fuel rod with the porous highly Zr-enriched “hot” center, apparently dense Zr-depleted intermediate zone, and slightly Zr-enriched “cold” outer zone [5, 6]. Diffusion data and thermodynamic properties of the U-Zr alloys are very important for understanding phenomena occurring in the fuel rods under irradiation. Ogata *et al.* [7] demonstrated that the interdiffusion coefficients of the γ -U-Zr solid solutions are closely related to the thermodynamic properties of this system. That is why in order to study redistribution of Zr in the U-Zr fuel rod one should perform, as the first step, *ab initio* calculations of the decomposition curve for the γ -U-Zr system, and calculate its basic ground-state properties. In this paper we present results of these calculations.

Another remarkable feature of the U-Zr system is the δ -UZr₂ phase, which solidifies in a modified C32 (AlB₂)-type crystal structure. It is well known that the high-temperature Zr- or Ti-based solid solutions may transform into the so-called metastable ω -phase at low temperatures [8]. The ω -phase became a subject of numerous experimental and theoretical studies since it was discovered more than fifty years ago because of its unique technological applications. This phase can also be stabilized from the α (hcp) phase of Zr (Ti) under compression [8, 9]. According to the X-ray and high resolution neutron diffraction structure analysis of the UZr₂ compound [4, 10], Zr atom occupies the “Al” position (0, 0, 0) of the hexagonal cell in the (AlB₂)-type crystal structure and a random mixture of U and Zr atoms occupies the “B” positions ($\frac{2}{3}$, $\frac{1}{3}$, $\frac{1}{2}$) and ($\frac{1}{3}$, $\frac{2}{3}$, $\frac{1}{2}$). Akabori *et al.* [11] performed interdiffusion coefficients measurements in the δ -UZr₂ phase by means of an electron-probe micro-analyzer, and found them to be significantly smaller than those extrapolated from the γ -U-Zr solid solutions [7] to the δ -phase. Finally, Ogawa *et al.* [12] suggested that the δ -UZr₂ intermediate phase could be regarded as an ω -phase solid solution that is stabilized against the α -Zr (hcp) structure by addition of U due to increase of the Zr *d*-band occupancy. In this paper we present results of calculations of the ground-state properties of the δ -UZr₂ phase and verified the hypothesis of this stabilization suggested in Ref. [12].

In our calculations we employ three complementary computational techniques: (i) scalar-relativistic Green’s function technique based on the Korringa-Kohn-Rostoker (KKR) method within the atomic-sphere approximation (ASA), (ii) the scalar-relativistic exact muffin-tin orbital method (EMTO), and (iii) the all-electron full-potential linear muffin-tin orbital method (FPLMTO) that accounts for all relativistic effects. Pertinent

details of the computational methods are described in Section 2. Results of density-functional calculations of the ground-state properties of the μ -based U-Zr solid solution and the decomposition curve are presented in Section 3. Section 4 is dedicated to the study of the δ -UZr₂ phase. In Section 5 we revisit a hypothesis of δ -phase stabilization due to increase of the Zr-*d*-band occupancy in the U-Zr system. Lastly, concluding remarks are presented in Section 6.

2. Computational details

The calculations we have referred to as KKR-ASA are performed using the scalar relativistic (no spin-orbit coupling) Green's function technique based on the KKR method within the atomic-sphere approximation [13-15]. Here ASA is improved by addition of higher multipoles of the charge density [15], and the so-called muffin-tin correction [16] to the electrostatic energy. The calculations are performed for a basis set including valence *spdf* orbitals and the semi-core *6p* states for uranium whereas the core states are recalculated at every iteration (soft-core approximation). For the electron exchange and correlation energy functional, the generalized gradient approximation (GGA) is adopted [17]. Integration over the Brillouin zone is performed using the special *k*-point technique [18] with 506 and 576 points in the irreducible wedge of the zone for the bcc and hcp structure, respectively. The moments of the density of states, needed for the kinetic energy and valence charge density, are calculated by integrating Green's function over a complex energy contour (with a 2.5 Ry diameter) using a Gaussian integration technique with 30 points on a semi-circle enclosing the occupied states. The

equilibrium density of the U-Zr system is obtained from a Murnaghan [19] fit to about ten total energies calculated as a function of the lattice constant.

In order to treat compositional disorder the KKR-ASA method is combined with the coherent potential approximation (CPA) [20]. The ground-state properties of the random U-Zr alloys are obtained from KKR-ASA-CPA calculations with the Coulomb screening potential and energy [21, 22]. The screening constants, α and β (see, for example, eq. (6) in Ref. [23]), are determined from supercell calculations using locally self-consistent Green's function method (LSGF) [24]. For the U-Zr alloys the α and β screening constants are found to be 0.70 and 1.06, respectively. The effective cluster interactions (ECI), used in Monte Carlo (MC) simulations, are obtained from the screened generalized-perturbation method (SGPM) [21, 22, 25].

Though the KKR-ASA formalism is well suited to treat close-packed structures it could produce a significant error when being applied to 'open' structures such as C32. That is why we use another Green's function technique, based on the EMT formalism, in present calculations, which is not limited by geometrical restrictions imposed by the ASA.

The EMT calculations are performed using scalar-relativistic Green's function technique based on the improved screened KKR method, where the one-electron potential is represented by optimized overlapping muffin-tin (OOMT) potential spheres [26, 27]. Inside the potential spheres the potential is spherically symmetric, and it is constant between the spheres. The radii of the potential spheres, the spherical potentials inside the spheres, and the constant value from the interstitial are determined by minimizing (i) the deviation between the exact and overlapping potentials, and (ii) the errors coming from

the overlap between spheres. Within the EMTO formalism, the one-electron states are calculated exactly for the OOMT potentials. As an output of the EMTO calculations, one can determine self-consistent Green's function of the system and the complete, non-spherically symmetric charged density. Finally, the total energy is calculated using the full charge-density technique [28]. Like in the case of KKR-ASA calculations, GGA is used for the electron exchange and correlation approximation, EMTO is combined with the CPA for calculation of the total energy of chemically random alloys; integrations over the Brillouin zone and complex energy contour, the choice of the screening constants are identical to those in the KKR-ASA method, except that, within the EMTO formalism, we can study the C32 structure and integration over the Brillouin zone for this structure is performed with 81 k -points in the irreducible wedge of the zone.

For the elemental metals, the most accurate and fully relativistic calculations are performed using an all-electron approach where the relativistic effects, including spin-orbit coupling, are accounted for. Although unable to model disorder in the CPA sense it provides important information for the metals, and also serves to confirm the CPA calculations mentioned above. For this purpose we use a version of the FPLMTO [29-31]. The "full potential" in FPLMTO refers to the use of non-spherical contributions to the electron charge density and potential. This is accomplished by expanding the charge density and potential in cubic harmonics inside non-overlapping muffin-tin spheres and in a Fourier series in the interstitial region. We use two energy tails associated with each basis orbital, and for U's semi-core $6s$, $6p$ states and valence states ($7s$, $7p$, $6d$, and $5f$) these pairs are different. With this 'double basis' approach we use a total of six energy tail parameters and a total of 12 basis functions per atom. Spherical harmonic expansions

are carried out up to $l_{max}=6$ for the bases, potential, and charge density. As in the case of the KKR-ASA and EMT methods, GGA is used for the electron exchange-correlation approximation. A special quasi-random structure (SQS) method was used to treat the compositional disorder within the FPLMTO formalism [32].

3. Ground-state properties and decomposition curve of the γ U-Zr solid solutions

Figures 1 (a-c) show results of KKR-ASA calculations of the equilibrium volume, Grüneisen constant, heat of formation of the γ U-Zr solid solutions, as well as the bulk modulus and Debye temperature. The lattice vibration effects are accounted for within the so-called Debye-Grüneisen quasi-harmonic model [33, 34] and here evaluated at 300 K. Both equilibrium volume and heat of formation of the γ U-Zr solid solutions show a positive deviation from Vegard's law that agrees well with the existence of a miscibility gap in the U-Zr phase diagram. One should notice that calculated heats of mixing of the γ U-Zr solid solutions are in excellent agreement with data extracted from the experimental phase diagram by the use of CALPHAD methodology [35], which indicates the robustness of the *ab initio* approach used in the present calculations. For comparison, we also show the heats of formation of the γ U-Zr for the $U_{75}Zr_{25}$, $U_{50}Zr_{50}$, and $U_{25}Zr_{75}$ alloys calculated within FPLMTO-SQS technique.

We performed MC calculations of the decomposition curve for the γ U-Zr solid solutions. Calculations are performed with an Ising-type representation of chemical order within the canonical ensemble. The MC simulations are performed using the Metropolis algorithm [36] for a 1728-site simulation box ($12 \cdot 12 \cdot 12$) with periodic boundary conditions. Set of pair (V^2), 3-site (V^3), and 4-site (V^4) ECI are obtained from SGPM

calculations performed at the theoretical equilibrium lattice constant (see Figure 1) for each composition of $\gamma\text{U}_{(1-c)}\text{Zr}_c$ alloys under consideration. For example, the calculated lattice parameter for the $\gamma\text{U}_{30}\text{Zr}_{70}$ alloy is 3.588 Å that coincides with the experimental measured value of 3.589 Å at the $\gamma\delta$ transition temperature $T = 925$ K [10]. The proximity of the calculated lattice constant of the $\gamma\text{U-Zr}$ alloys, used for the determination of ECI for subsequent MC simulations, and actual values of the lattice constant, measured in the vicinity of the decomposition of the γ phase, indicates a good chance of successfully reproducing this phase transformation with our simulations.

Figure 2 shows the first nine effective pair interactions (EPI) calculated for the $\gamma\text{U}_{1-c}\text{Zr}_c$ alloys. A significant negative value of the 1st and 2nd nearest-neighbor EPI's suggests a strong tendency toward phase separation in this system. Figure 3 shows the total energy per atom and its temperature derivative obtained from MC simulations for the $\gamma\text{U}_{90}\text{Zr}_{10}$ alloy. This plot also indicates the critical temperature of the phase transformation, T_c , in this alloy.

Figure 4 displays the calculated temperature of decomposition of the $\gamma\text{U}_{1-c}\text{Zr}_c$ alloys within the wide range of composition. This curve has a maximum that is located somewhere between 20 and 30 at. % of Zr. This maximum matches relatively well the location of the maximum on the experimental miscibility gap (~ 30 at. % Zr) also shown in the figure. However, calculated temperature of decomposition of the $\gamma\text{U-Zr}$ solid solutions significantly exceeds the experimental value of the miscibility gap. To explain this discrepancy, we show calculated temperature dependence of the heat of formation of these solutions in Figure 5. A significant decrease of the heat of formation with temperature implies that the temperature dependence of the ECI should be accounted for

in our MC simulations. This temperature dependence is considered within the following simple scheme [38]. Let us introduce the excess vibrational free energy for the $A_cB_{(1-c)}$ alloy

$$\Delta F_{\text{alloy}}^{\text{vibr.}} = F_{\text{alloy}}^{\text{vibr.}} - \left[cF_{\text{A}}^{\text{vibr.}} + (1-c)F_{\text{B}}^{\text{vibr.}} \right], \quad (1)$$

where c is the composition in A species. Within the regular solution approximation

$$\Delta F_{\text{alloy}}^{\text{vibr.}} = c(1-c)P, \quad (2)$$

and the coefficient P is associated with the EPI (for simplicity), V_i^2 , on the i^{th} coordination sphere:

$$P = -\frac{1}{2} \sum_i Z_i V_i^2, \quad (3)$$

where Z_i refers to a coordination number. If, for simplicity, the only 1st coordination shell is considered, one has

$$P = -\frac{1}{2} Z_1 V_1^2, \quad (4)$$

where Z_l and V_l^2 are the coordination number and the EPI associated with the 1st coordination shell, respectively. Thus, from Esq. (2) and (4) one can get the vibrational contribution of the nearest-neighbor EPI to the free energy according to

$$\Delta F_{\text{alloy}}^{\text{vibr.}} = -\frac{1}{2}c(1-c)Z_1V_1^2. \quad (5)$$

Using eq. (1) for the excess vibrational free energy for the $A_cB_{(1-c)}$ alloy, one can estimate the ‘thermal’ correction to the nearest-neighbor EPI.

Figure 6 shows the temperature dependence of the nearest-neighbor EPI calculated for several alloy compositions of γ U-Zr. This correction substantially decreases the calculated temperature of the decomposition of γ U-Zr alloys (see Figure 4) in comparison with the previously discussed MC results performed without thermal correction to the EPI’s. One should also mention that the calculated transition temperature, $T_c \approx 1020$ K, for the γ U₉₀Zr₁₀ alloy, shown in Figure 3, corresponds to MC simulations performed with the thermally corrected nearest-neighbor EPI. Thermal effects associated with the next-neighbor EPI’s should cause further decrease of the calculated decomposition curve.

4. Ground-state properties of the δ UZr₂ compound

Figure 7 shows the C32 (AlB₂) structure. It has two non-equivalent types of sublattice with 3 atoms per unit cell: sublattices of “Al-” (one site) and “B-” (two sites) types. The actual arrangement of U and Zr atoms in δ UZr₂ phase, has been widely discussed, see,

e.g., Refs. [3, 4], and the last uncertainties were removed by careful high-resolution neutron diffraction measurements [10]. As we mentioned in the Introduction, it is now believed that in the δUZr_2 compound Zr atoms occupy the Al-type position (0, 0, 0) of the hexagonal cell, and a random mixture of U and Zr atoms occupies the B-type positions $(\frac{2}{3}, \frac{1}{3}, \frac{1}{2})$ and $(\frac{1}{3}, \frac{2}{3}, \frac{1}{2})$. To confirm that this arrangement is actually the ground-state configuration of the δUZr_2 compound, we performed EMTO calculations of the equilibrium lattice constant for three atomic configurations of the C32 structure: (i) random distribution of U and Zr atoms on each of the three sites (the $\text{U}_{1/3}\text{Zr}_{2/3}$ “disordered” alloy); (ii) “complete” ordering with U atoms occupying the Al-type sublattice and Zr atoms occupying the B-type sublattice; (iii) “partial” ordering that corresponds to experimental observation described above. Figure 8 shows the total energy of the δUZr_2 compound, in 3 configurations, (i) – (iii), as a function of the Wigner-Seitz radius. One can see that the two types of ordering, “complete” and “partial”, are energetically favorable in comparison with the disordered configuration, however, a) the configuration (iii) has the lowest total energy (ground-state) and b) the equilibrium lattice constant for the configuration (ii) significantly exceeds the experimentally observed lattice parameter of the δUZr_2 compound [4]. Indeed, according to Table 5 of Ref. [4], the experimental lattice parameters for the δUZr_2 compound with 66.9 at. % Zr are: $a = 5.025 \text{ \AA}$ and $c = 3.086 \text{ \AA}$, which corresponds to the volume of the unit cell $V = a^2 c \frac{\sqrt{3}}{2} = 67.4837 \text{ \AA}^3$ and the volume per atom $\Omega = \frac{V}{3} = 22.4946 \text{ \AA}^3$ resulting in the Wigner-Seitz radius

$$S_{WS} = \sqrt[3]{\frac{3\Omega}{4\pi}} = 1.7512 \text{ \AA} = 3.3093 \text{ a.u.}. \text{ According to our calculations, the equilibrium}$$

Wigner-Seitz radius is 3.317 a.u., 3.375 a.u., and 3.295 a.u., for configurations (i), (ii), and (iii), respectively, which strongly suggests that configurations (i) and (iii), described within EMTO formalism, are most realistic.

We have also calculated the enthalpy of formation of the δ -UZr₂ compound. We define this property as

$$\Delta H_f = E_{\text{UZr}_2}^{C32} - \left[\frac{1}{3} E_U^\alpha + \frac{2}{3} E_{\text{Zr}}^\alpha \right], \quad (6)$$

where $E_{\text{UZr}_2}^{C32}$ is the energy of the δ -UZr₂ compound and E_U^α and E_{Zr}^α are the energies of α -U and α -Zr, respectively. Present calculations reveal $E_{\text{UZr}_2}^{C32} = -6.29$ kJ/mol that is in fair agreement with experimental measurements of -4.0 kJ/mol at $T = 298$ K [39, 40].

5. Stability of the δ -phase in the U-Zr system

It is well established that under compression zirconium metal undergoes the following phase transformations: α -Zr (hcp) \rightarrow ω -Zr (C32) \rightarrow β -Zr (bcc) [8, 9, 41-43]. We performed FPLMTO calculations of the total energy of α -, ω -, and β -Zr phases as functions of atomic volume and results of these calculations are shown in Figure 9. According to the present calculations, the $\alpha \rightarrow \omega$ and $\omega \rightarrow \beta$ phase transitions in Zr take place at 33 and 268 kbar, respectively, which are in a good accord with experimental measurements (see Table). One should also notice the significant scattering of the experimental data, especially for the $\alpha \rightarrow \omega$ transition.

Figure 10 (a) shows the s -, p -, and d -band occupations in α -Zr as a function of the Wigner-Seitz radius (FPLMTO calculations). As the Wigner-Seitz radius decreases (e.g., with increase of pressure), the occupation of the d -band goes up due to a loss of the s and p electrons. In Figure 10 (b) we show the structural-energy difference obtained from canonical bands [44] as a function of d -band filling. One can see that as soon as the Zr d -band occupation increases under compression, hcp gradually transforms, initially to C32, and then to bcc. For the C32 (ω) phase, this plot is very different than that published by Ahuja *et al.* [45]. The reason for the difference is that the present results in Figure 10 (b) are obtained from canonical band energies with the repulsive contribution, due to overlapping orbitals, included. This contribution becomes increasingly important for open crystal structures (such as C32) [46] and was not included in Ref. [45].

Next, we discuss the analogies with the U-Zr system. Figure 11 has two parts. The upper part shows how the d -band occupation of α -Zr changes under compression, and the transition region (full black) spans between the lower and upper experimental bounds, 21 kbar and 85 kbar (see Table), of the $\alpha \rightarrow \omega$ transformation. The hatched patch of the upper part of the plot shows the pressure region of the certain ω -phase stability in pure Zr. The lower part of this plot shows how the d -band occupation of changes as a function of an increase in U composition in the U-Zr system. The hatched part of this part of the plot spans within the range of the homogeneity of the δ -U-Zr phase (18 – 37 at. % U [4]). One can see that at the upper pressure border of the $\alpha \rightarrow \omega$ phase transition range in pure Zr (~ 85 kbar) its d -occupation almost reaches the same value as it has when composition of U, alloyed with α -Zr, reaches the value (~ 18 at. %, [4]) when the δ -UZr₂ phase starts to form. Thus the present calculations confirm the hypothesis of Ref. [12] according to

which the stabilization of the δUZr_2 phase in the U-Zr system has the same origin as that of the ω -phase in pure zirconium under compression, namely, it is induced by an increase in d -band filling.

6. Conclusion.

Due to progressive use of metallic fuels in fast breeder reactors it becomes very important to understand factors that shape performance of these fuels. There are a lot of factors that determine materials performance, e.g., degree of fuel swelling due to fission products and transmutant elements, swelling due to irradiation damage and gas release, fuel-cladding mechanical and chemical interactions, fuel constituent redistribution and zone formation, fuel volume change due to element segregation and phase change, changes to coefficients of thermal expansion, lanthanide fission product migration, redistribution of minor actinides, mechanical integrity (development of cracks and voids), etc. [1]. To study these complex phenomena it is important, first of all, to predict the thermodynamic properties of actinide-based materials used in fast breeder reactors, e.g., U-Pu-Zr (base material), solutes (Np, Am, Cm), as well as transition metals (Mo, Ta, W) for subsequent studies of fuel cladding interaction. The phenomenological thermochemical CALPHAD approach [35] is the available tool in alloy processing modeling with wide predictive capabilities. By integrating CALPHAD methodology with *ab initio* technique one can efficiently predict the thermodynamic properties of actinides and their alloys with further studies on mechanical and chemical stabilities of metallic fuels, and aging, corrosion, and wear resistance properties.

In the present paper *ab initio* results on equilibrium properties are obtained for U-Zr alloys to understand the effectiveness of *ab initio* methods in describing actinide alloys. Ground-state properties of γ U-Z solid solutions and the δ UZr₂ compound were calculated. Predicted temperature of decomposition of γ U-Zr alloys is in a reasonable agreement with the γ -phase miscibility gap. Stabilization of the δ UZr₂ phase in the U-Zr system is explained in terms of an increase in *d*-band occupancy by the addition of U to Zr. These *ab initio* results will be used to build a completely theoretical phase diagram that can be compared with experimental and CALPHAD phase diagrams. This will serve as a template to investigate a mixture of U and Pu with minor actinides for which experimental data are lacking. In a near future, this improved and validated coupling between *ab initio* and CALPHAD methodologies will allow us to predict the thermodynamic driving force, associated with any actinide-based alloy, and this will be used as an input for predicting microstructure evolution and site redistribution, and validate the development of the phenomenological potentials for subsequent molecular dynamics simulations.

Acknowledgements

This work was performed under the auspices of the US Department of Energy by Lawrence Livermore National Laboratory under contract DE-AC52-07NA27344. A. Landa would like to thank Drs. A. Ruban and L. Vitos for helpful discussions.

References:

1. G.L. Hofman, L.C. Walters, T.H. Bauer, Progr. Nucl. Energy (1/2) (1997) 83-110.

2. D.D. Keiser, Jr., J.B. Kennedy, B.A. Hilton, S.L Hayes, JOM (1) (2008) 29-32.
3. T. Ogawa, T. Iwai, J. Less-Comm. Met. 170 (1991) 101-108.
4. M. Akabori, A. Itoh, T. Ogawa, F. Kobayashi, Y. Suzuki, J. Nucl. Mater. 188 (1992) 249-254.
5. T. Ogawa, T. Iwai, M. Kurata, J. Less-Comm. Met. 175 (1991) 59-69.
6. G.L. Hofman, S.L. Hayes, M.C. Petri, J. Nucl. Mater. 227 (1996) 277-286.
7. T. Ogawa, M. Akabori, A. Itoh, T. Ogawa, J. Nucl. Mater. 232 (1996) 125-130.
8. S.K. Sikka, Y.K. Vohra, R. Chidambaran, Prog. Mater. Sci. 27 (1982) 245-310.
9. H. Xia, A.L. Ruoff, Y.K. Vohra, Phys. Rev. B 44 (1991) 10374-10376.
10. M. Akabori, T. Ogawa, A. Itoh, Y. Morii, J. Phys.: Condensed Matter 7 (1995) 8249-8257.
11. M. Akabori, A. Itoh, T. Ogawa, T. Ogata, J. Alloys Comp. 271-273 (1998) 597-601.
12. T. Ogawa, J.K. Gibson, R.G. Haire, M.M. Gensini, M. Akabori, J. Nucl. Mater. 223 (1995) 67-71.
13. O. Gunnarson, O. Jepsen, O.K. Andersen, Phys. Rev B 27 (1983) 7144-7168.
14. I.A. Abrikosov, H.L. Skriver, Phys. Rev B 47 (1993) 16532-16541.
15. A.V. Ruban, H.L. Skriver, Comput. Mater. Sci. 15 (1999) 119-143.
16. N.E. Christensen, S. Satpathy, Phys. Rev. Lett. 55 (1985) 600-603.
17. J.P. Perdew, K. Burke, M. Ernzerhof, Phys. Rev. Lett. 77 (1996) 3865-3868.
18. D.J. Chadi, M.L. Cohen, Phys. Rev. B 8 (1973) 5747-5753; Phys. Rev B 39 (1989) 3168-3172.
19. F.D. Murnaghan, Proc. Natl. Acad. Sci. U.S.A. 30 (1944) 244-247.

20. J.S. Faulkner, Prog. Mater. Sci. 27 (1982) 1-187.
21. A.V. Ruban, H.L. Skriver, Phys. Rev. B 66 (2002) 02420-1-115.
22. A.V. Ruban, S.I. Simak, P.A. Korzhavyi, H.L. Skriver, Phys. Rev. B 66 (2002) 024202-1-12.
23. A.V. Ruban, S.I. Simak, S. Shallcross, H.L. Skriver, Phys. Rev. B 67 (2003) 214302-1-12.
24. I.A. Abrikosov, S.I. Simak, B. Johansson, A.V. Ruban, H.L. Skriver, Phys. Rev. B 56 (1997) 9319-9334.
25. A.V. Ruban, I.A. Abrikosov, Rep. Prog. Phys. 71 (2008) 046501-1-30.
26. L. Vitos, Phys. Rev B 64 (2001) 014107-1-11.
27. L. Vitos, Computational Quantum Mechanics for Materials Engineers: The EMT0 Method and Application, Springer, London, 2007.
28. J. Kollar, L. Vitos, H.L. Skriver, in: H. Dreyssé (Ed.), Electronic Structure and Physical Properties of Solids: The Uses of the LMTO Method, Lecture Notes in Physics, Springer, Berlin, 2000, pp. 85-113.
29. J.M. Wills, B. Cooper, Phys. Rev. B 36 (1987) 3809-3823.
30. D.L. Price, B. Cooper, Phys. Rev. B 39 (1989) 4945-4957.
31. J.M. Wills, O. Eriksson, M. Alouani, D.L. Price, in: H. Dreyssé (Ed.), Electronic Structure and Physical Properties of Solids: The Uses of the LMTO Method, Lecture Notes in Physics, Springer, Berlin, 2000, pp.148-167.
32. A. Zunger, S.H. Wei, L.G. Ferreira, J.E. Bernard, Phys. Rev. Lett. 65 (1990) 353-356.
33. V.L. Moruzzi, J.F. Janak, K. Schwartz, Phys. Rev. B 37 (1988) 790-799.

34. P. Söderlind, L. Nordström, L. Yongming, B. Johansson, Phys. Rev B 42 (1990) 4544-4552.
35. P.E.A. Turchi, I.A. Abrikosov, B. Burton, S.G. Fries, G. Grimvall, L. Kauffman, P. Korzhavyi, V. Rao Manga, M. Ohno, A. Pisch, A. Scott, W. Zhang, CALPHAD 31 (2007) 4-27.
36. K. Binder, Application of the Monte Carlo Method in Statistical Physics, Springer, Berlin, 1987.
37. H. Okamoto, J. Phase Equilib. 14 (2) (1993) 267-268.
38. A.V. Ruban, private communication (2007).
39. K. Nagarajan, R. Babu, C.K. Mathews, J. Nucl. Mat. 203 (1993) 221-223.
40. T. Ogawa, J. Nucl. Mat. 209 (1994) 107-108.
41. S.A. Ostanin, V.Yu. Trubisin, Phys. Rev. 57 (1998) 13485-13490.
42. Y. Akahama, M. Kobayashi, H. Kawanura, J. Phys. Soc. Jap. 60 (1991) 3211-3214.
43. C.W. Greeff, Modeling Simul. Mater. Sci. Eng. 13 (2005) 1015-1027.
44. H.L. Skriver, Phys. Rev. B 31 (1985) 1909-1923.
45. R. Ahuja, J.M. Wills, B. Johansson, O. Eriksson, Phys. Rev. B 48, (1993) 16269-16279.
46. P. Söderlind, J.M. Wills, O. Eriksson, Phys. Rev. B 57 (1998) 1320-1323.

Captions

Figure 1. The bulk modulus and Debye temperature (a); the heat of formation (b); the atomic volume and Grüneisen constant (c) of the γ U-Zr alloys.

Figure 2. The first nine effective pair interactions for the γ U-Zr alloys.

Figure 3. The total energy and its temperature derivative as a function of temperature in Ising-type MC simulations of the γ U-Zr alloys.

Figure 4. Temperature of decomposition of the γ U-Zr alloys. Experimental data on the miscibility gap are taken from Ref. [37].

Figure 5. Temperature dependence of the heat of formation of the γ U-Zr alloys.

Figure 6. Temperature dependence of the nearest neighbor coordination shell interaction for the γ U-Zr alloys.

Figure 7. The C32 (AlB₂) structure. Al-type and B-type atoms are colored dark and light grey, respectively.

Figure 8. The total energy of the δ -UZr₂ compound for (i) - (iii) configurations (see text) as a function of the Wigner-Seitz radius. The equilibrium energy of the “partially” order configuration is used as the reference point and is set equal to zero.

Figure 9. The total energy of hcp, C32, and bcc Zr as a function of the atomic volume.

Figure 10. The change in band occupancy in Zr under compression (a); the energy difference, obtained from canonical d -bands, as a function of d -band occupancy (b). The hcp energy is used as the reference point and is set equal to zero.

Figure 11. Comparison of d -band occupancy in α -Zr as a function of compression with d -band occupancy in the U-Zr alloys as a function of U concentration.

Table. Experimental and theoretical (FPLMTO) pressure of the $\alpha \rightarrow \omega$ and $\omega \rightarrow \beta$ phase transitions in Zr.

Source	$\alpha \rightarrow \omega$ transition (kbar)	Source	$\omega \rightarrow \beta$ transition (kbar)
Ref. [8]	21 - 60	Ref. [9]	320
Ref. [41]	33 - 67	Ref. [42]	330
Ref. [43]	23 - 85	Ref. [43]	240 - 310
FPLMTO	33	FPLMTO	268

Figures.

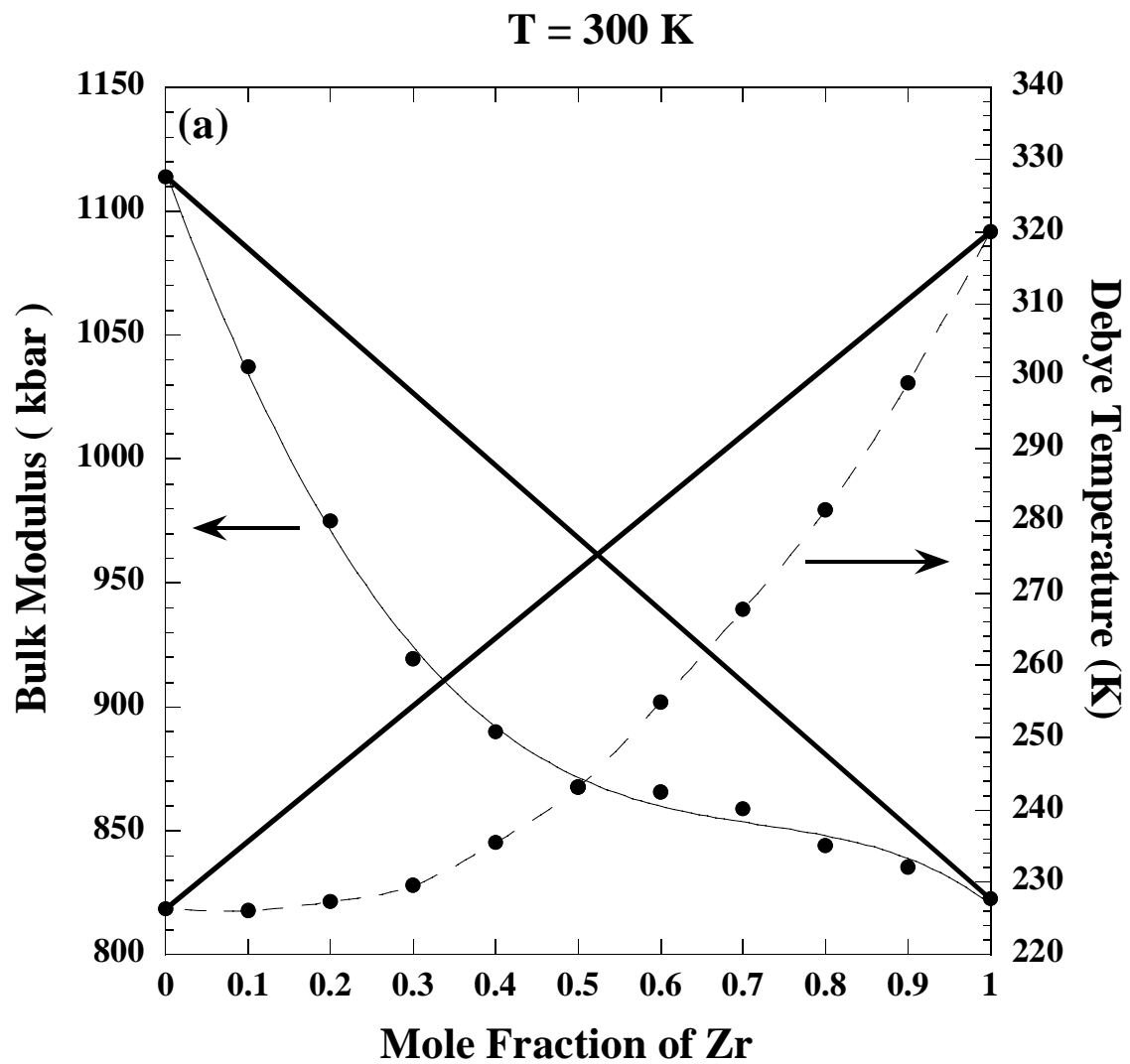


Figure 1a.

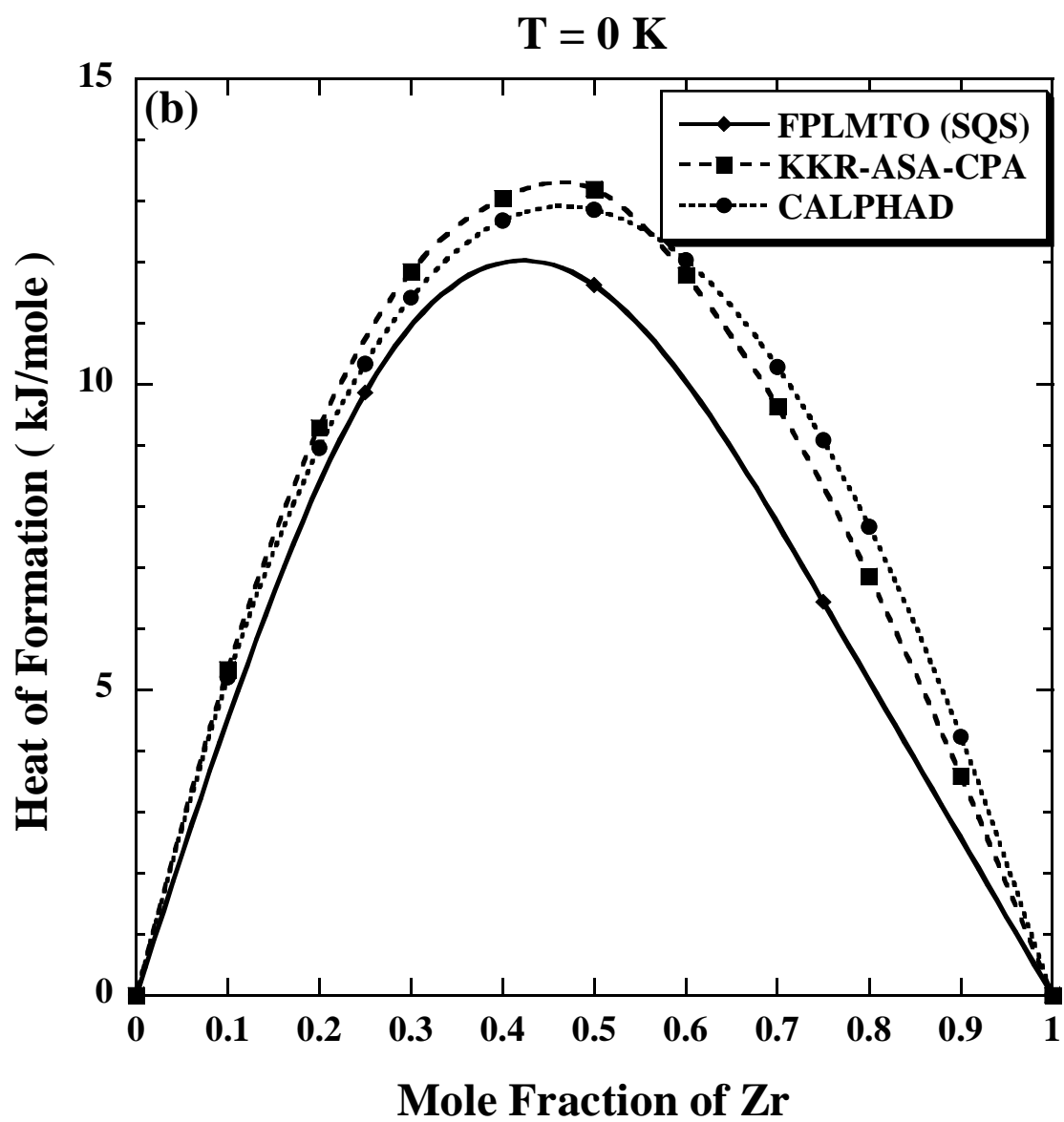


Figure 1 b.

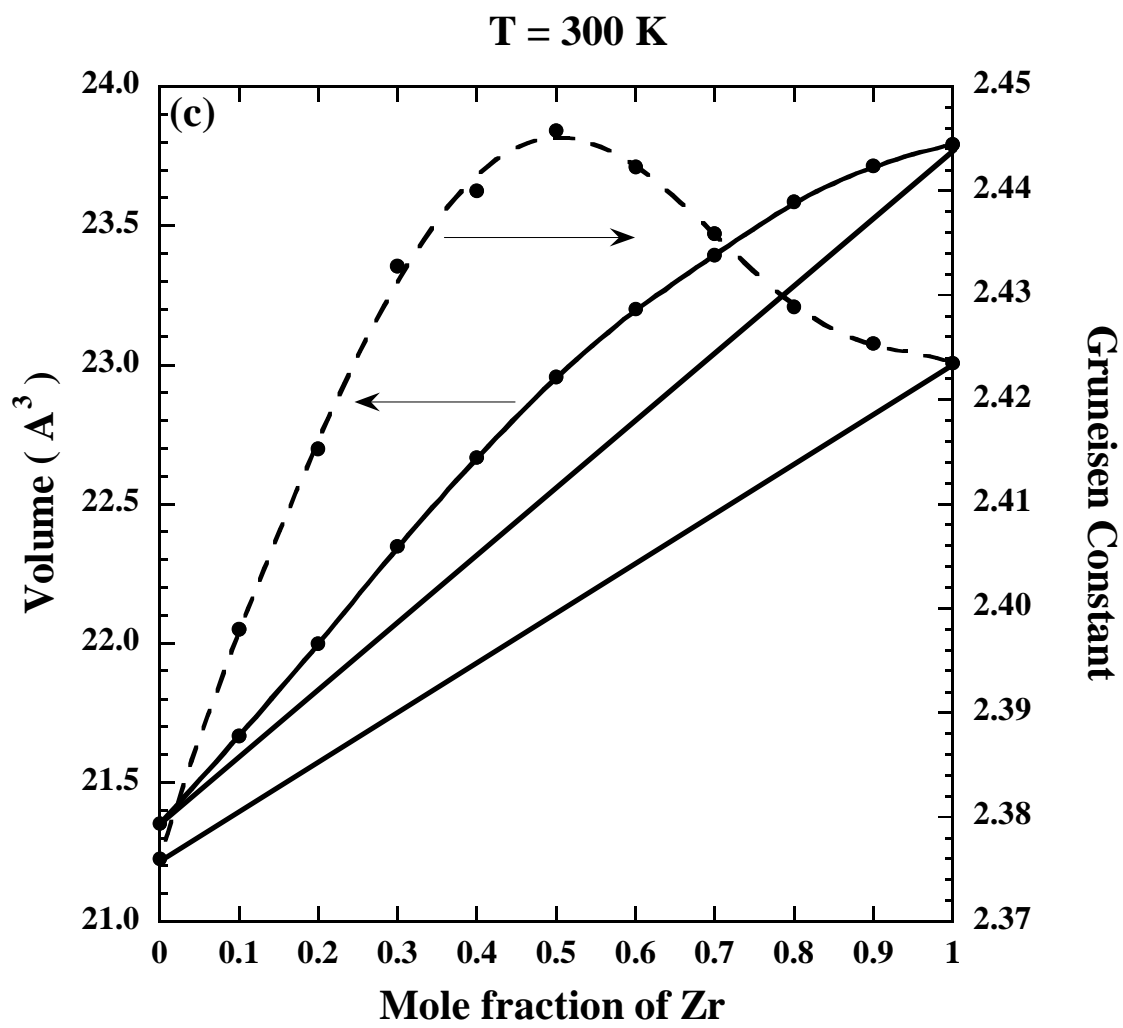


Figure 1c.

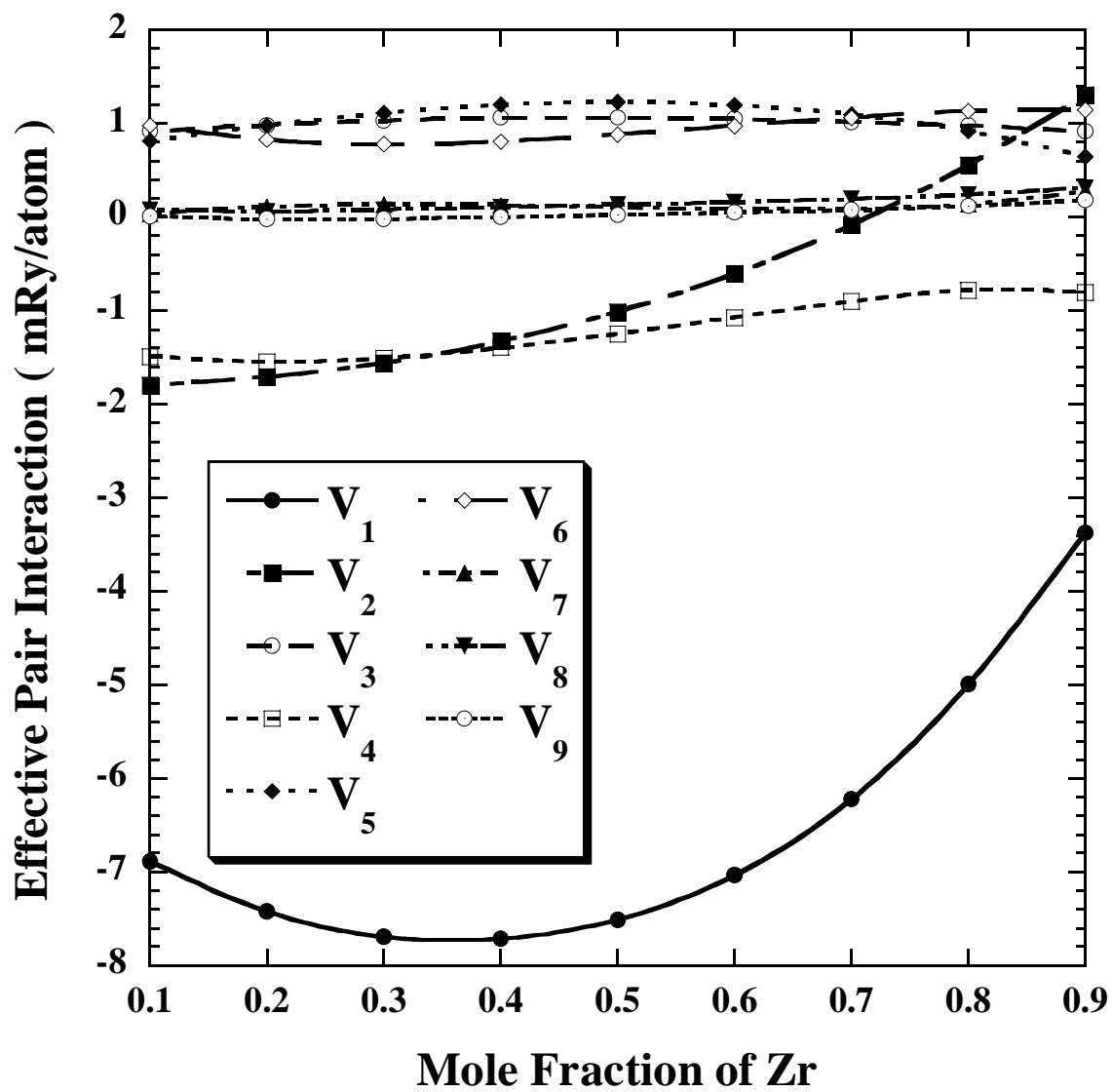


Figure 2.

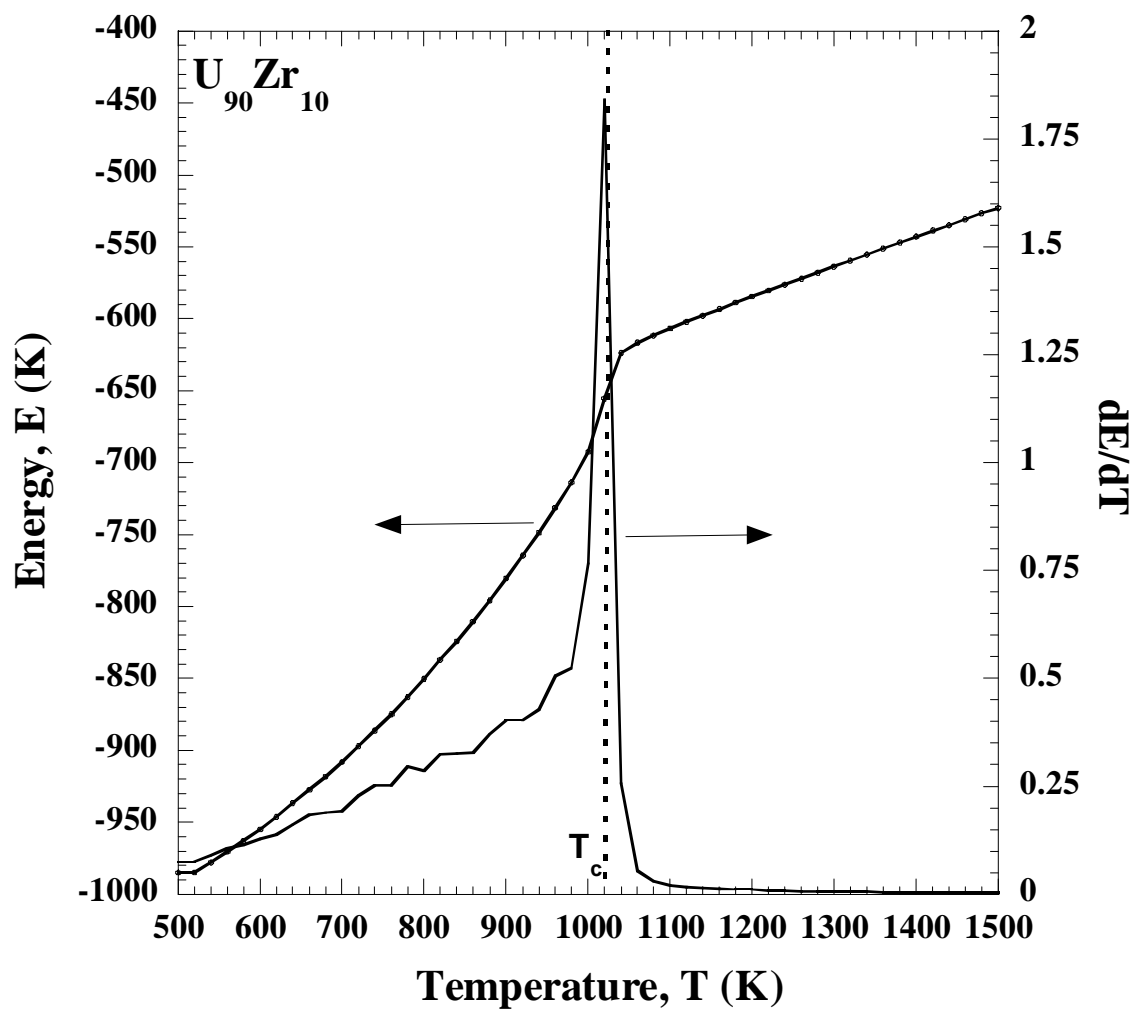


Figure 3.

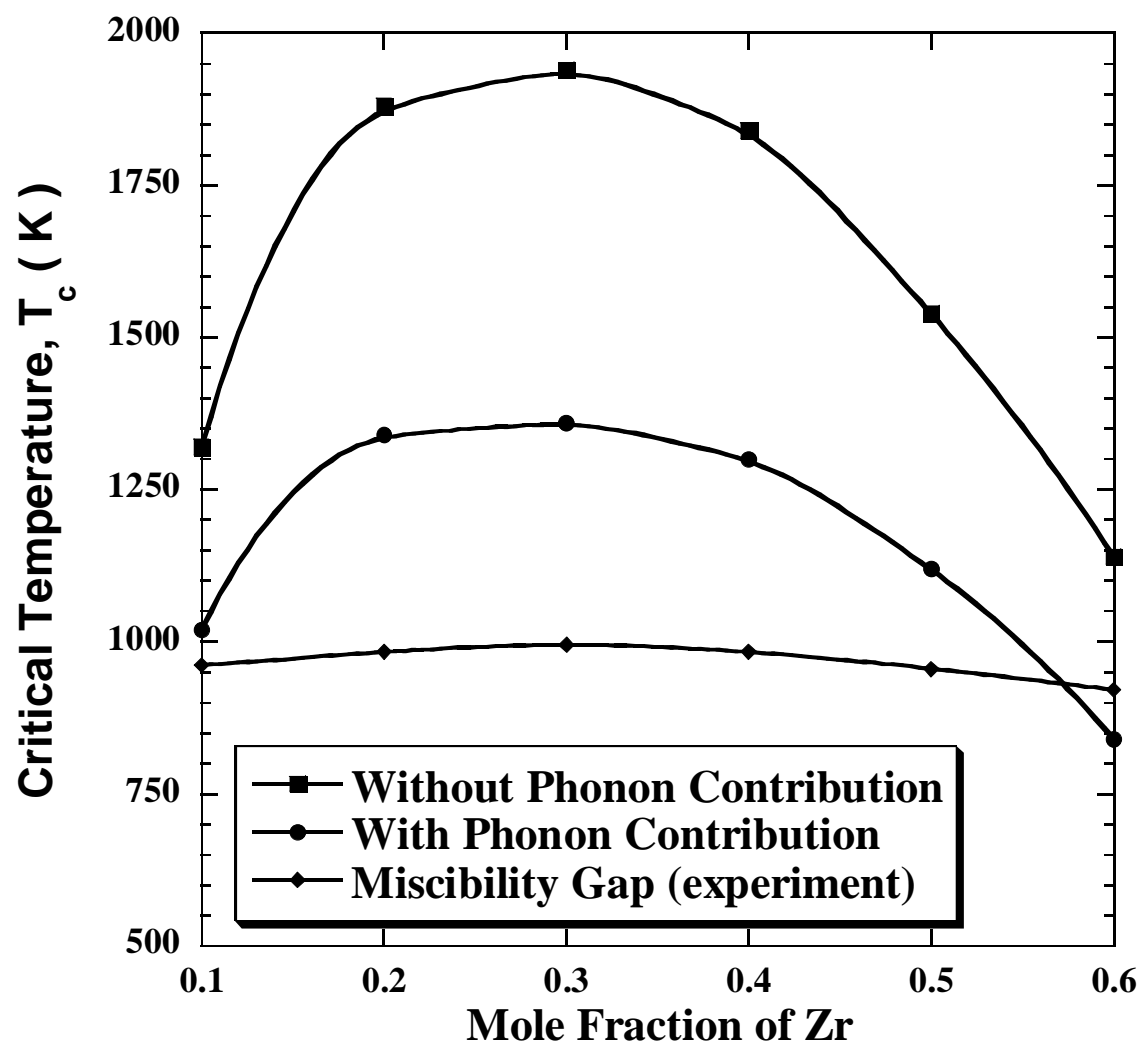


Figure 4.

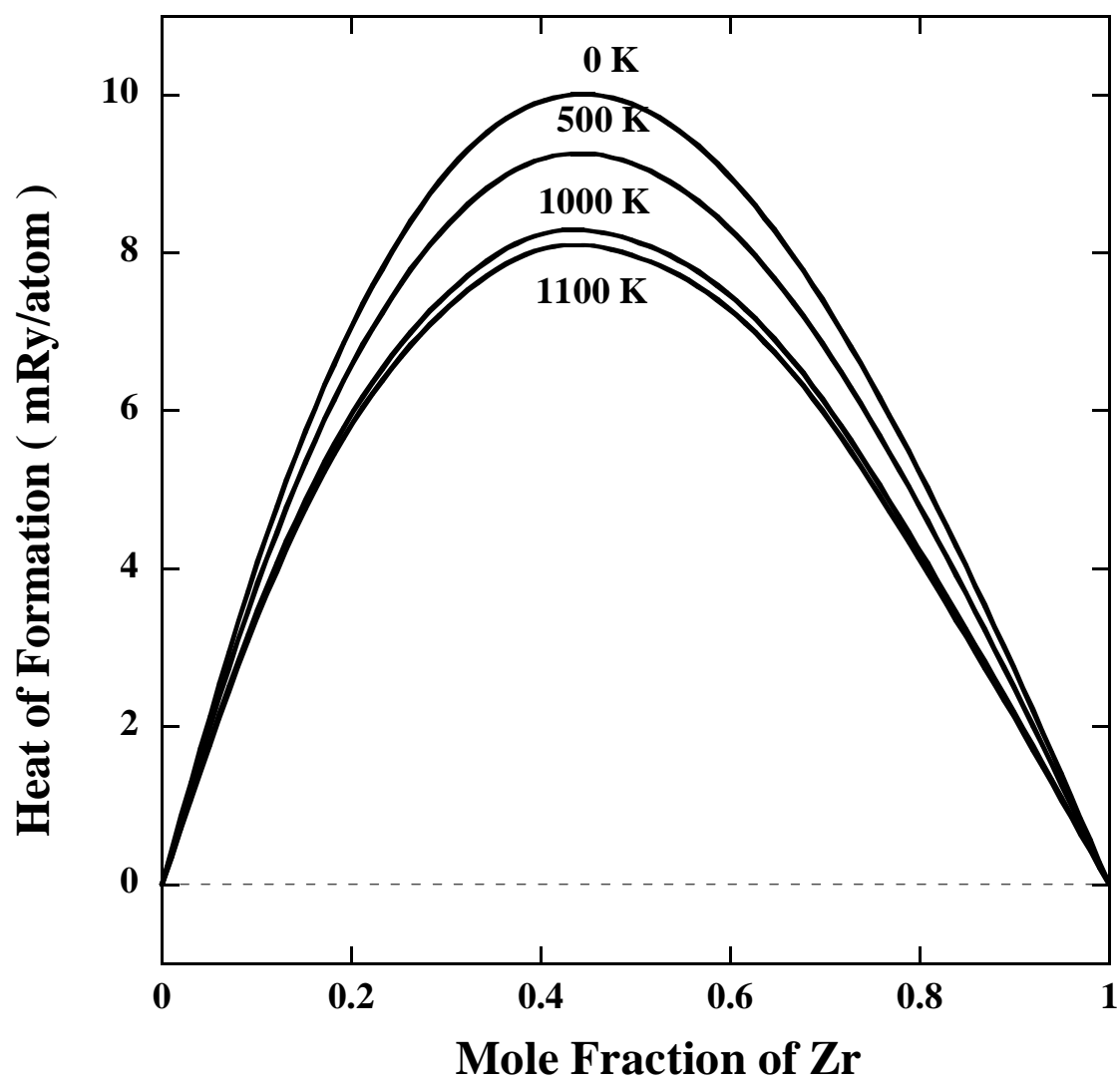


Figure 5.

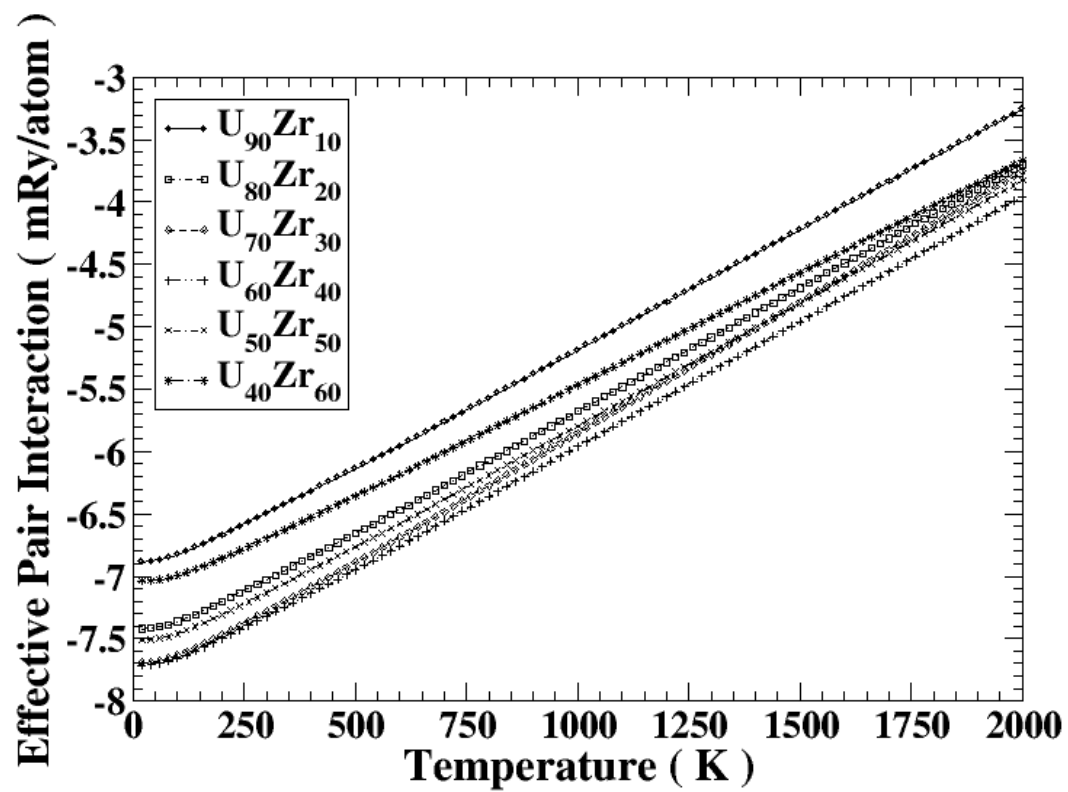


Figure 6.

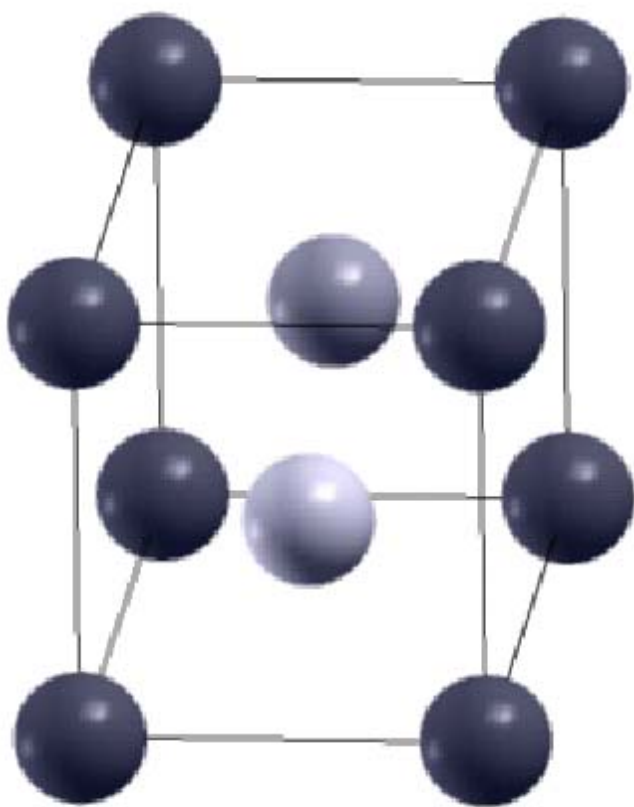


Figure 7.

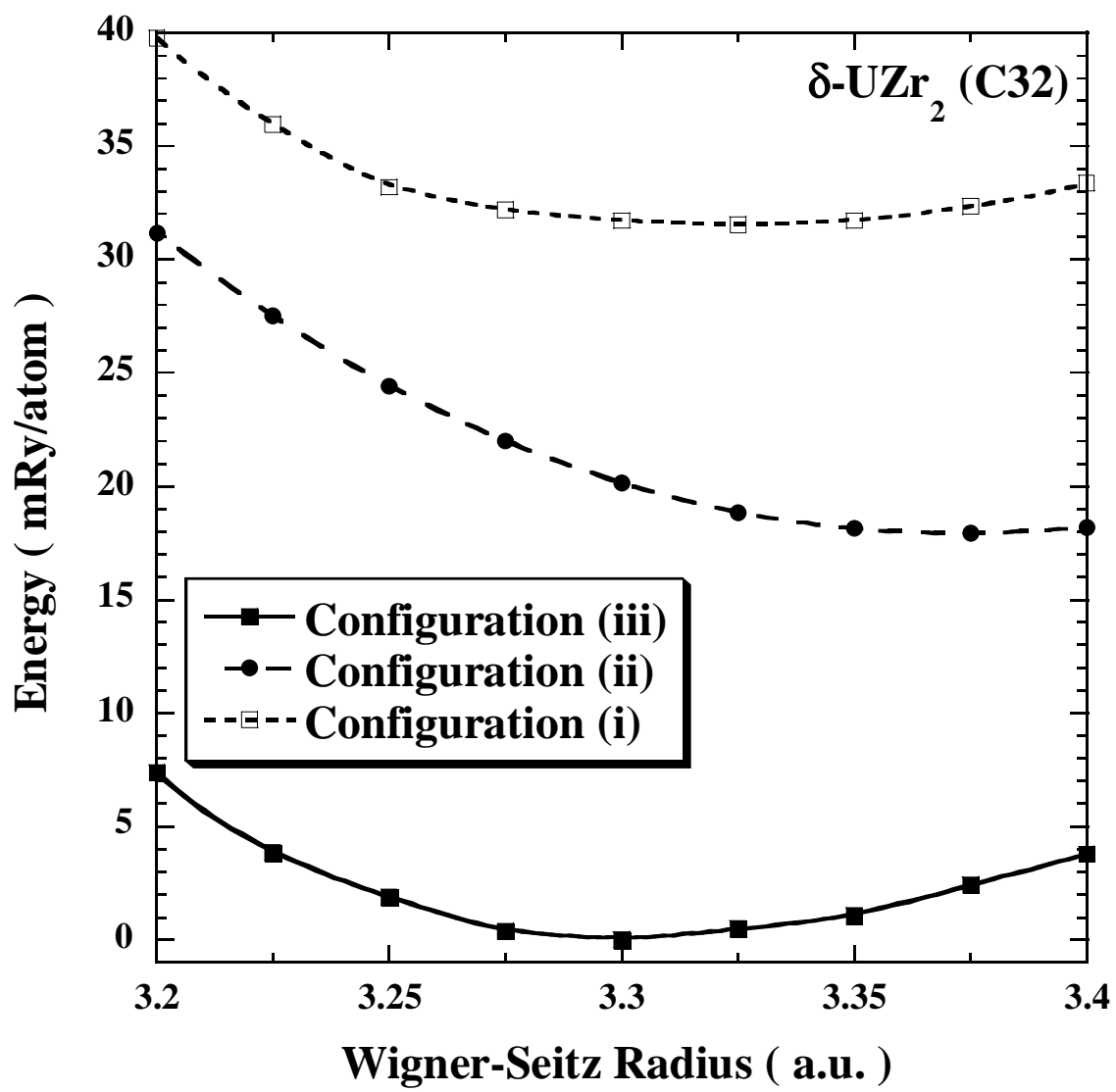


Figure 8.

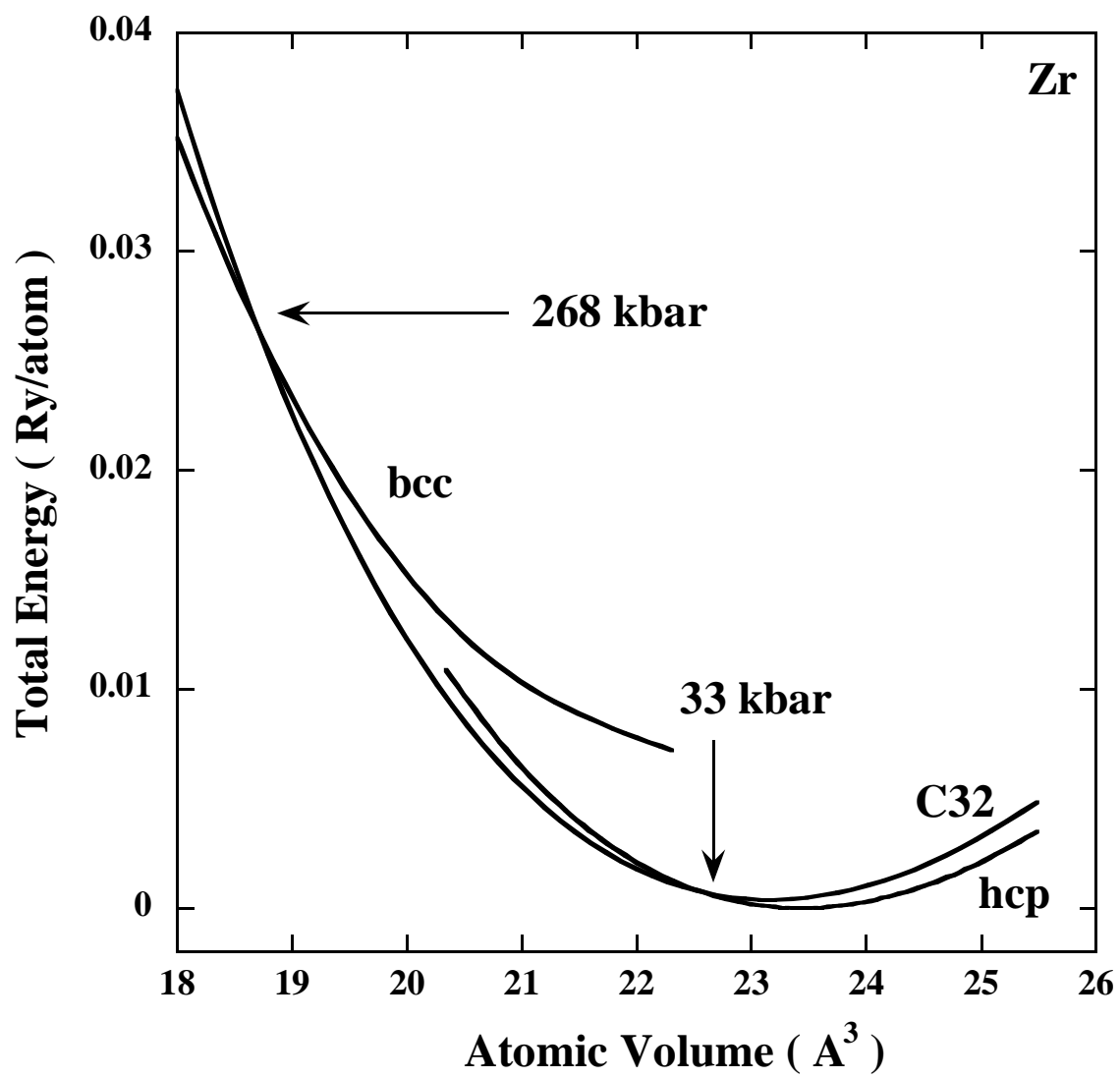


Figure 9.

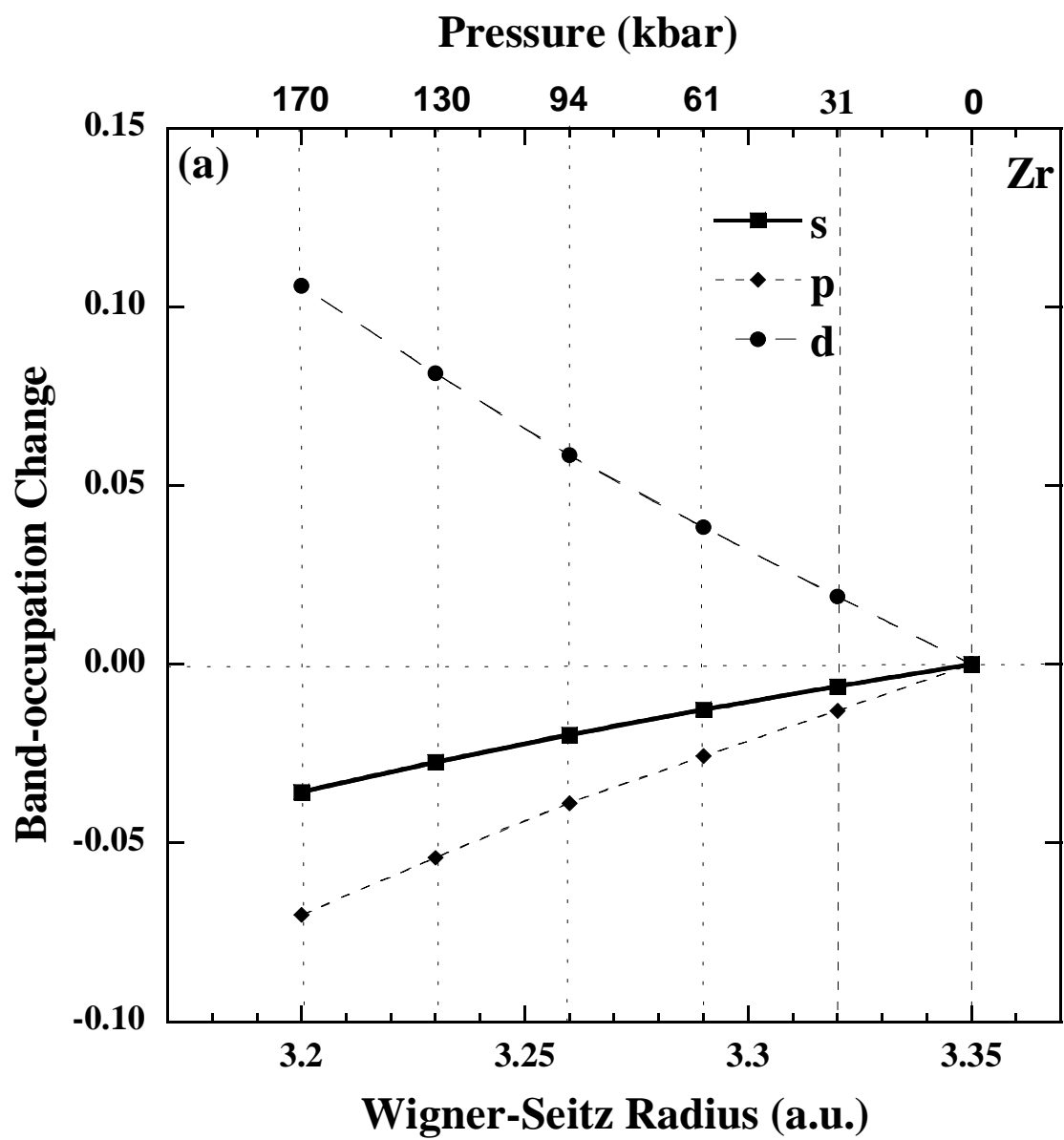


Figure 10 a.

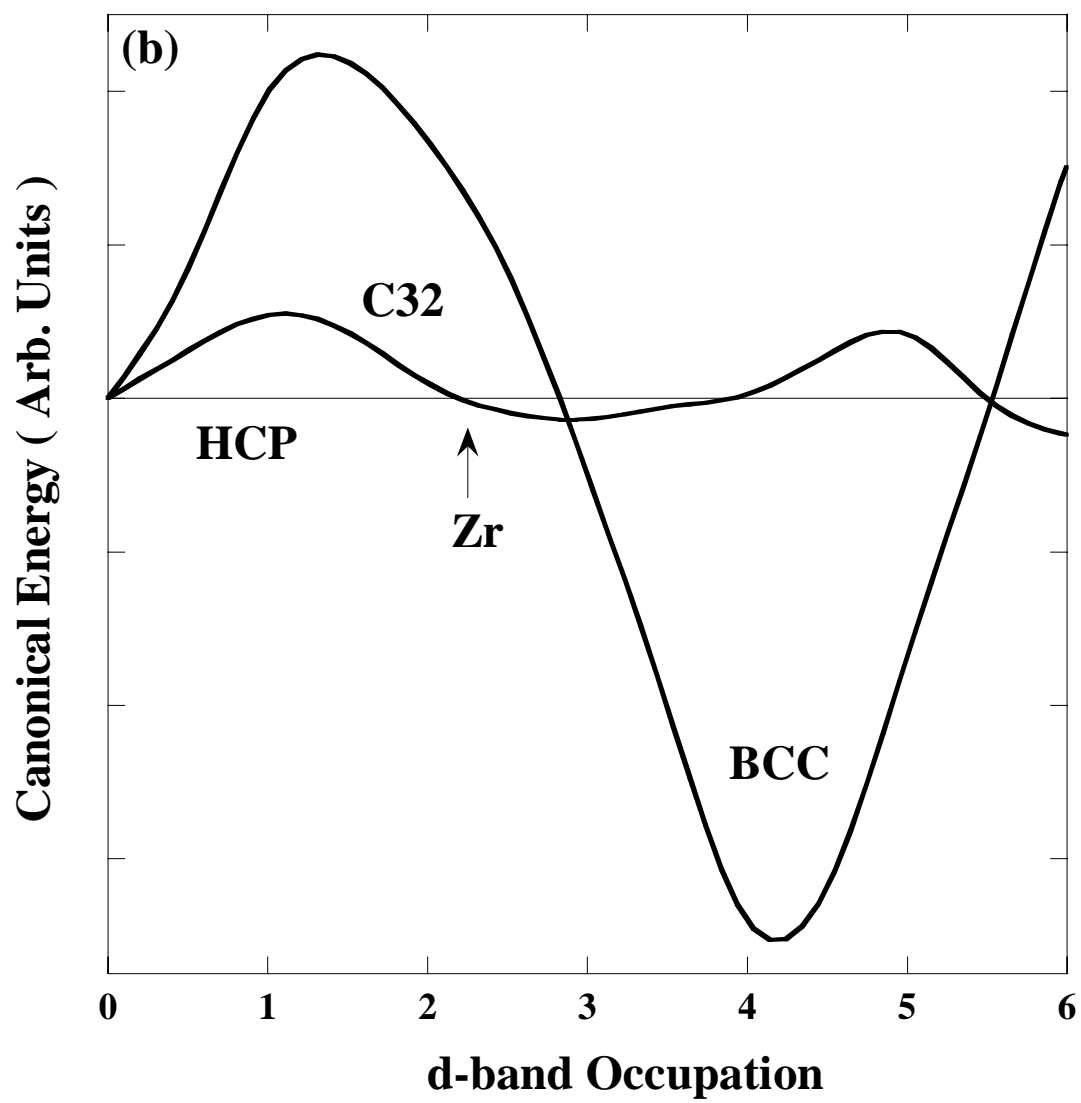


Figure 10 b.

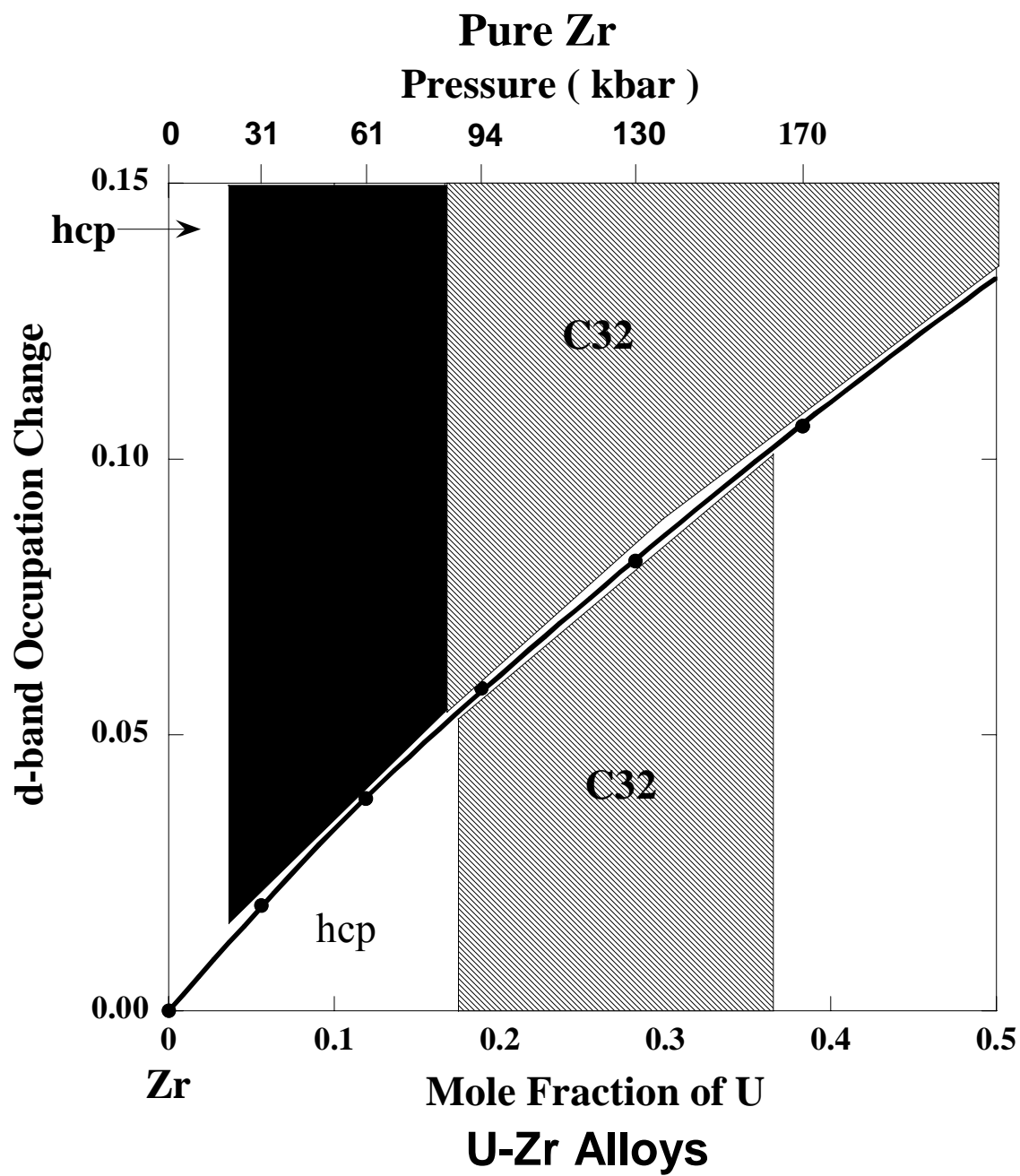


Figure 11.